Composites Part A 109 (2018) 84–94

Contents lists available at ScienceDirect

Composites Part A

journal homepage: www.elsevier.com/locate/compositesa

Laser-based surface patterning of composite plates for improved secondary adhesive bonding

Ran Tao[a], Marco Alfano[b], Gilles Lubineau[a,*]

[a] King Abdullah University of Science and Technology (KAUST), Physical Sciences and Engineering Division (PSE), COHMAS Laboratory, Thuwal 23955-6900, Saudi Arabia

[b] Department of Mechanical, Energy and Management Engineering, University of Calabria, 87036 Rende, CS, Italy

ARTICLE INFO

Keywords:
Adhesive joints
CFRP
Fracture toughness
Pulsed laser irradiation
Patterned interface

2010 MSC:
00-01
99-00

ABSTRACT

The effects of laser irradiation surface pretreatments on the mode I fracture toughness of adhesively bonded composite joints were evaluated. First, pulsed CO_2 laser irradiation was uniformly deployed on carbon fiber reinforced polymer (CFRP) substrates. Next, double cantilever beam (DCB) tests were performed to assess the effects of surface pretreatments on the mode I fracture toughness of the adhesive joints. Then, a thoughtful combination of the proposed surface pretreatments was deployed to fabricate DCB specimens with patterned interfaces. A wide range of techniques, including X-ray photoelectron spectroscopy (XPS), contact profilometry, and optical and scanning electron microscopy (SEM) were used to ascertain the effects of all investigated surface pretreatments. It is shown that patterning promoted damage mechanisms that were not observed in the uniformly treated interfaces, resulting in an effective fracture toughness well above that predicted by a classical rule of mixture.

1. Introduction

Lightweight materials play a very important role in the aerospace industry. Several large-scale aviation structures (*e. g.* fuselages, wings, fan blades, tail cones) are made up of carbon fiber-reinforced polymers (CFRPs) [1]. The key to affordability of the composite structures is reducing assembly costs [2]. However, joining remains a major cost in aerospace manufacturing due to the different properties of CFRPs with respect to metallic materials. Traditional mechanical fastenings, *e. g.*, rivets or bolts, have several shortcomings. The hole-locating, drilling, and fastener installation process are among the main labor-intensive activities in aircraft construction and rework. In addition, rivets and bolts add significantly to the total structural weight. Because of recent developments in structural adhesive technologies and surface preparation techniques, secondary adhesive bonding has the potential to replace riveting and bolting in the joining of cured composites [3–8]. The use of adhesives instead of rivets and bolts has been shown to reduce structural weight, facilitate a wide range of material combinations, and provide uniform stress distribution, thereby reducing the risk of fatigue failure [9]. The major concern which arises in adhesive bonding of composites is the requirement of suitable surface pretreatments able to prevent the adverse effect of surface contaminants and favor the adhesion at the adhesive/CFRP interface. Efficient surface pretreatments should enhance the strength and fracture toughness of composite joints by promoting chemical bonding (*e. g.*, physical adsorption, covalent bonding) and mechanical interlocking [9–18]. Common pretreatments include mechanical sandblasting (or sanding) and applying peel-plies to the surfaces of composites. The final objective of these techniques is mainly to remove contaminants (*e. g.*, mold release agents), but also to increase the surface polarity, surface energy, and contact area of the adhesive/CFRP interface. Surface contamination in the form of mono-layer adsorbates may prevent adhesion at the adhesive/CFRP interface and induce adhesive failure. However, sandblasting is labor-intensive for large structures and exhibits two main areas of concern: the non-uniformity and the inherent trade-off between the full removal of contamination and damage of surface fibers. The use of peel-ply minimizes the human error present in sandblasting [11]; moreover, it is attractive from a manufacturing and quality assurance standpoint because it reduces manufacturing costs, ensures good reproducibility, is easy to apply, and protects the surface during handling prior to bonding [11,15]. However, the peel-ply-treated surface very often needs to be cleaned or activated [15].

Since aerospace applications require robust, repeatable, and reliable processes, additional strategies have been devised through the years, such as wet chemical treatments [3,14,17] and physical high-energy radiation treatments which include, for example, plasma [13,19,20]

* Corresponding author.
E-mail addresses: marco.alfano@unical.it (M. Alfano), gilles.lubineau@kaust.edu.sa (G. Lubineau).

https://doi.org/10.1016/j.compositesa.2018.02.041
Received 1 November 2017; Received in revised form 26 January 2018; Accepted 27 February 2018
Available online 01 March 2018
1359-835X/

and laser processing [8,9,13,18]. Photo-grafting and surface functionalization are commonly employed chemical treatments to enhance interfacial adhesion, promote covalent bonding, and improve the shear strength and fracture toughness of composite joints [14,17]. However, similar to sandblasting, chemical treatments may cause harm to the environment by producing large amounts of (hazardous) chemical waste. Moreover, chemical treatments are difficult to automate in an industrial scenario. Modern high-energy radiation treatments provide an environmentally friendly alternative to wet chemical treatments. Plasma is widely used process which has been proved to enhance the strength and fracture toughness of adhesively bonded composite joints, especially after aging. However, plasma processing usually provides little or no modification of surface morphology and does not enable mechanical interlocking of the bonding substrates [13]. Pulsed laser irradiation recently gained a lot of attention because it is a fast and controllable technique, which can simultaneously modify surface chemistry and morphology, and is suitable for large-scale applications [10,12,16,21–23]. In particular, laser beams can be used to selectively remove target materials, including potential contaminants. Laser treatments also reduce the risks associated with manual processing, *e. g.*, contamination and process variation. Currently, there is no universally defined tool for laser ablation; indeed, pulsed laser systems operate at different pulse regimes with wavelengths varying from UV to IR, which causes different interactions with the target material. For applications on CFRPs, previous works focused on excimer ($\lambda = 308$ nm) [12,21], Nd-YAG ($\lambda = 355$ nm) [16,18], fiber lasers (near-IR range, $\lambda = 1064$ nm) [24] and CO_2 lasers (mid-IR range, $\lambda = 10.6$ μm) [9,23,25]. The different laser-CFRP interactions that can be realized lead to large variations in the treated surfaces, from a simple surface "cleaning", with little or no modification of surface layers, to a full removal of the matrix with consequent exposure of carbon fibers. As a consequence, these surfaces lead to very different fracture responses. Compared to UV lasers, CO_2 laser has higher processing speed and larger processing area, which is suitable for industrial applications [23]. Besides, fiber lasers input larger amount of heat into carbon fibers, resulting in near surface substrate damage such as the fiber/matrix debonding [9,25].

In this work, in a quest to fabricate composite joints with superior fracture properties, thoughtful combinations of different uniform CO_2 laser surface treatments are deployed to generate CFRP substrates with patterned interfaces. The effects of uniform (*i. e.* no pattern) laser irradiation pretreatments on the mode I fracture toughness of adhesively bonded composite joints were firstly evaluated in comparison with peel-ply and sandblasting pretreatments. A wide range of techniques, including X-ray photoelectron spectroscopy (XPS), contact profilometry, and optical and scanning electron microscopy (SEM) were used to ascertain the features of the pretreated CFRP interfaces. The corresponding fracture toughness was assessed through double cantilever beam (DCB) tests and the fracture surfaces were analyzed through both the optical microscopy and SEM. Finally, the DCB specimens with patterned interfaces were analyzed and comparative analyses were carried out.

2. Materials and methods

2.1. Material

The substrate materials were unidirectional carbon fiber pre-pregs composed of toughened epoxy resin and carbon fibers (HexPly T700/M21, Hexcel, Stamford, CT, USA), with a nominal fiber volume of 57%, which represents an aerospace-grade composite material. Unidirectional laminates ($[0°]_8$) were fabricated by compression molding to work as substrates for the following adhesive bonding. The curing cycle of the laminates was conducted as follows. First, a full vacuum (1 bar) was applied to every four-layer stacking in order to reduce air entrapment and void formation in the final laminate. Then, a gauge pressure (7 bar) was applied using a hydraulic hot press machine (Hydraulic presses, Pinette Emidecau Industries, Chalon-sur-Saone, France) at a heating rate of 3 °C/min and a hold time of 120 min at 180 °C. Finally, the laminate was cooled at a rate of 3 °C/min.

The adhesive selected for bonding the cured CFRP substrates was a two component room-temperature curing epoxy (Araldite 420 A/B, Huntsman, Salt Lake City, UT, USA). It is a structural adhesive with high shear and peel strengths for bonding materials such as metals, thermosets, and thermoplastics. The basic mechanical properties of the adhesive provided by the manufacturer and obtained through tensile tests are given as follows: Young's modulus, $E = 1.5$ GPa; elongation at break, $\epsilon_f = 4.6\%$; and tensile strength, $\sigma_f = 29$ MPa [26].

2.2. Surface pretreatments

A commercial polyamide (dry) peel-ply (Diatex PA85, Diatex, Saint-Genis-Laval, France) was applied to the pre-preg stacking to generate a standard surface condition for the subsequent comparative analyses. The peel-ply fabric, once removed before bonding, should generate a fresh and activated surface by removing excess resin. The peel-ply pretreatment will be referred to as *PP* in this study. The additional standard surface condition was obtained by sandblasting (*SB*) for the subsequent comparative analyses, which was performed using a wet blaster (Hurricane, MBA, CA, USA). Pulsed laser irradiation (*L*) was carried out using a 10.6 μm CO_2 laser (PLS6.75 Laser Platform, Universal Laser Systems, NY, USA). Different surface modifications were attained by controlling adjustable laser processing parameters in *L*, *e. g.*, the laser speed, average power, and pulse frequency. Since CFRP substrates may be produced with different surface-resin contents and fiber orientations, a careful evaluation of the laser processing parameters is necessary. The main parameter guiding the efficiency of the process is the pulse fluence (F_p):

$$F_p = I_p \cdot t_p = \frac{W_{ave}}{f \cdot A_s} = \frac{4W_{ave}}{v \cdot PPI \cdot \pi d^2}, \quad (1)$$

where I_p represents the laser irradiance, t_p is the laser pulse duration, $f = v \cdot PPI$ is the pulse frequency, W_{ave} is the average pulse power, $A_s = \pi d^2/4$ is the spot size, v is the beam traveling speed, and *PPI* represents the number of pulses per inch. Preliminary investigations revealed that the ablation depth depended on pulse fluence and frequency. In the present work, the pulse fluence F_p was elected as the controlling parameter of the ablation depth. Therefore, the average power was varied while the beam speed and number of laser pulses were kept constant at, $v = 500$ mm/s and $PPI = 1000$, respectively. The focal distance was adjusted so that the resulting laser spot diameter was $d = 200$ μm. In doing so, a light surface "cleaning" with minor modifications of surface roughness was achieved at a pulse fluence of $F_p = 1.2$ J/cm^2. This treatment, named *L*1, led to the ablation of the surface matrix and partially exposed carbon fibers. In addition, a higher pulse fluence, $F_p = 3.6$ J/cm^2, was deployed to fully expose carbon fibers. This treatment is referred to as *L*2. Nominally flat surfaces were obtained for the sandblasting and laser irradiation pretreatments by covering the pre-pregs with a Teflon film during curing. This baseline flat surface is referred to as *T*. Finally, all treated surfaces were degreased in an ultrasonic bath of acetone for 10 min, then oven-dried at 50 °C for 25 min before applying the epoxy adhesive.

2.3. XPS spectroscopy

XPS studies were carried out in a Kratos Axis Supra spectrometer (Amicus, Kratos Analytical Ltd, Manchester, UK) equipped with a monochromatic Al Ka X-ray source ($h\nu = 1486.6$ eV) operating at 300 W, a multichannel plate and delay line detector in a vacuum of 10^{-9} mbar. All spectra were recorded using an aperture slot of 300 μ m× 700 μm. The survey spectra were collected using a pass energy of 160 eV and a step size of 1 eV. A pass energy of 20 eV and a step size

of 0.1 eV were used for the high-resolution spectra. The samples were mounted in floating mode in order to avoid differential charging. Charge neutralization was required for all samples. Binding energies were referenced to the sp2 hybridized (C=C) carbon for the C1s peak set at 284.5 eV from CFRP laminates. The data were analyzed on commercial software (CASAXPS, Casa Software Ltd, Devon, UK).

2.4. Surface profilometry and high-resolution imaging

Surface profiles were measured by contact profilometry (Dektak 150 Surface Profiler, Veeco, New York, USA) using a microscopic stylus tip (5 μm radius). A minimum of five scans were carried out parallel and perpendicular to the fiber direction, featuring a gage length of 3 mm and a sampling resolution of 0.1667 μm/point. The arithmetical-average roughness (Eq. (2)) was extracted from the obtained profiles (R_a):

$$R_a = \frac{1}{n}\sum |y_i - y_{mean}|, \tag{2}$$

where n is the number of sampling points from each scan, y_i is the detrended height of the surface profile, and y_{mean} is the average of all y_i values. High-resolution SEM imaging (Quanta 600, FEI, CA, USA) was also deployed with secondary electrons to resolve the morphological features generated by the various pretreatments.

2.5. Determination of fracture toughness

Mode I fracture tests were carried out using the DCB configuration according to the procedures and recommendations reported in the ASTM D5528-13 standard ([27]). The CFRP laminates ($[0°]_8$) were bonded using the epoxy adhesive and a starter crack was generated using a nonadhesive polyethylene insert (60 mm long, 80 μm thick). Copper wires (100 μm diameter) were used as spacers to control the thickness of the adhesive layer. Mechanical pressure was applied during curing to ensure full adhesive-CFRP contact and a consistent thickness of the adhesive layer. Epoxy hardening was performed over 12 h in a temperature- and moisture-controlled laboratory environment, *i. e.* 22 °C and 71% R.H. The bonded plate was then cut into 250 × 20 × 4.1 mm^3 specimens and loading blocks were bonded onto each specimen's arm to enable the application of the end peel loading. A schematic of the as-obtained specimens is reported in Fig. 1. The figure also summarizes the investigated surface pretreatments. Mechanical tests were carried out under displacement control at a rate of 5 mm/min using a universal testing machine (Instron 5882, Instron, Massachusetts, USA). Loading and unloading cycles were employed during tests to prevent unstable crack propagation. The tests continued until the opening displacement reached 45 mm. The crack propagation was observed *in situ* using a high-resolution camera (Cannon EOS-1Ds, resolution 5616 × 3744 pixels) and with the aid of black lines at every millimeter marked on the specimen edge. The mode I fracture toughness (G_{Ic}) was averaged over at least five tests for each surface pretreatment. The compliance calibration (CC) method, suggested by the standard ASTM D5528-13 [27], was elected for the calculation of G_{Ic}:

$$G_{Ic} = \frac{nP\delta}{2ba}, \tag{3}$$

where P is the applied load, δ is the corresponding opening displacement, b is the specimen width, a is the crack length, and n is the CC term which was extracted from experimental data by means of a least-square plot of the logarithmic compliance as a function of the logarithmic crack length, *i. e.*, log(C)−log(a). Both the optical microscopy and SEM were deployed to probe the fracture surfaces and reveal the failure mechanisms.

3. Results and discussion

3.1. XPS spectroscopy

Global XPS surveys scans were performed, focusing on three main elements: C, O and Si. The resulting average atomic concentration of surface elements is given in the insert of Fig. 2. Fluorine (F) contamination was also detected, which could have been transferred from the Teflon film to the CFRP surface during curing; however, its atomic concentration was very limited (*i. e.*, 5%) compared to previous works (*i. e.*, 32%) [12]. Silicon, on the other hand, is a potential surface contaminant from molding release compounds, the product employed in the experiments, or the protective tape from the supplier. Small amounts of Si compounds are often added to pre-pregs as flame retardant, resulting in a baseline level of Si atomic concentration (*i. e.*, 0.4%) [28]. According to previous related work, Si may have a detrimental effect on the fracture toughness of adhesive/CFRP interfaces [29,30]. Besides, the atomic concentration of oxygen was reduced in the laser-treated samples with respect to the baseline *T* surfaces. Because of the low energy of the CO_2 laser photons, photo-chemical reactions are unlikely, and therefore, the reduction of oxygen could be

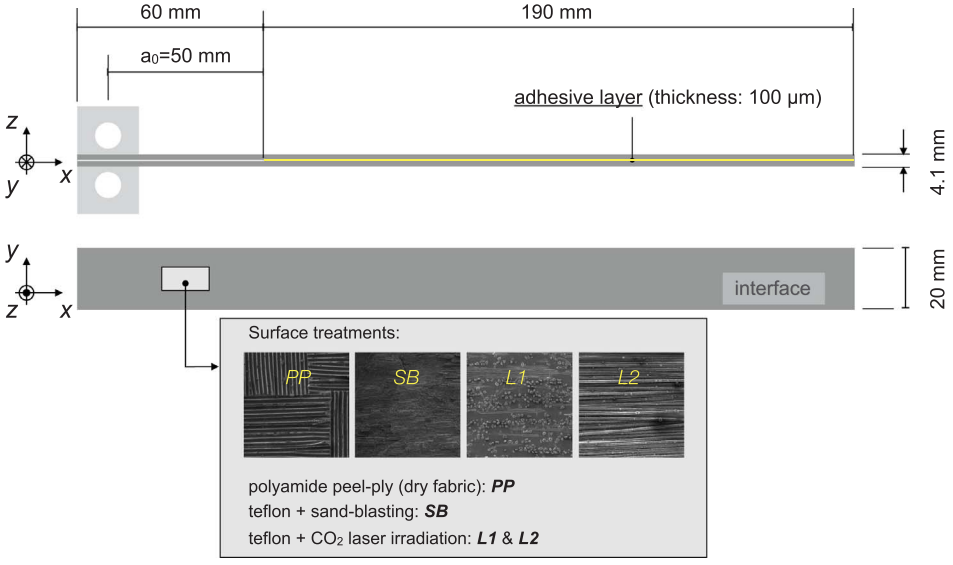

Fig. 1. Schematic depiction of the DCB specimens featuring the relevant geometrical dimensions and the investigated surface preparation strategies. The *x*-direction reflects the orientation of the carbon fiber. (For interpretation of the references to color in this figure legend, the reader is referred to the web version of this article.)

Treatment	atomic concentration %			concentration % of functional groups		
	C	O	Si	C-O alkoxy	C=O carbonyl	O-C=O carboxyl
PP	75.46	16.50	1.40	25.34	8.58	10.01
T	71.14	16.60	3.74	44.46	3.08	1.50
SB	76.38	16.68	0.74	51.32	0.94	2.39
L1	73.98	14.24	1.24	45.96	2.12	5.35
L2	82.98	12.34	0.36	52.90	4.11	7.97

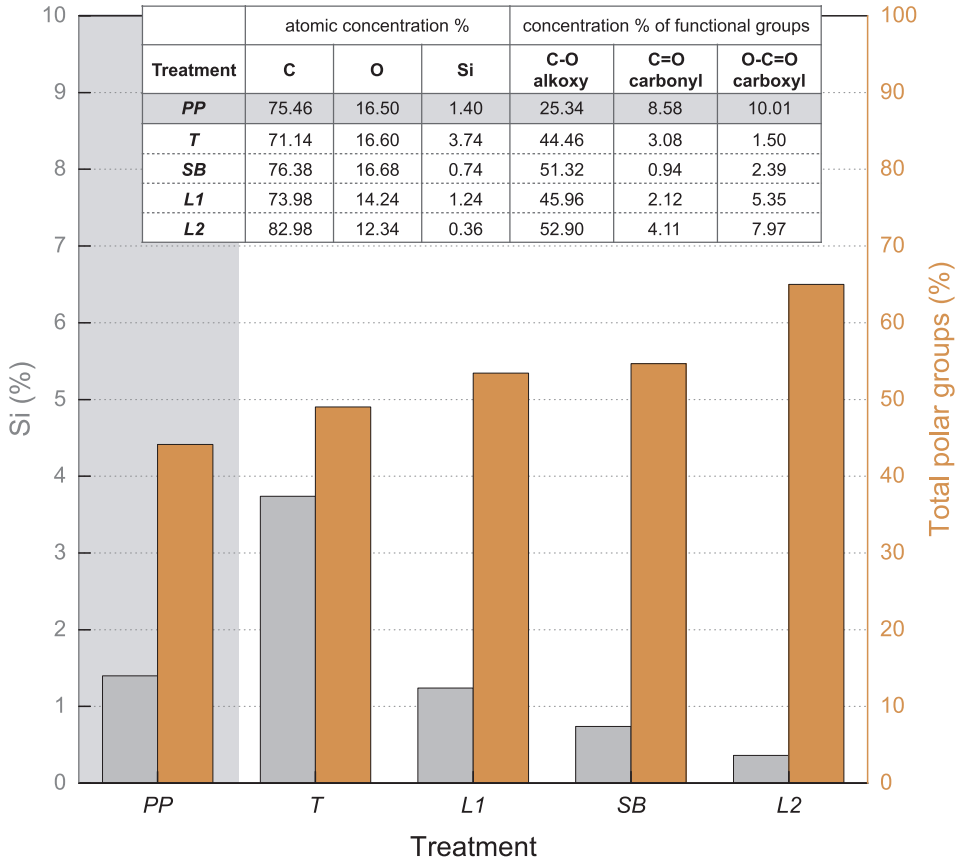

Fig. 2. Atomic concentration of elements and concentration of polar groups as obtained from XPS analyses. *PP*: peel-ply; *T*: Teflon; *L*1: laser irradiation at F_p = 1.2 J/cm^2; *SB*: sandblasting; and *L*2: laser irradiation at F_p = 3.6 J/cm^2. (For interpretation of the references to color in this figure legend, the reader is referred to the web version of this article.)

due to the removal of hydroxyl groups mainly through photo-thermal reactions [10].

High-resolution carbon peaks of C1s were assessed in the binding energy range from 277 to 304 eV to detect carbon-based surface functional groups. The results are listed in the insert of Fig. 2, where the concentration of functional groups was estimated from the area percentages of the fitted peaks from the C1s spectra. The following oxygen-containing groups were found: alkoxy (C—O), carbonyl (C═O), and carboxyl (O—C═O). All of these groups are correlated with the improvement of surface energy and wettability [13]. The total amount of polar groups is also listed in Fig. 2. An overall analysis of the data indicated that, starting from the baseline condition *T*, both the mechanical (*SB*) and physical surface treatments (*L*) reduced the Si contamination and also increased the polar groups. The residual Si in the laser-treated surfaces may have come from condensation during processing; while in sandblasting, the process may have merely smeared the Si contamination from one area to the other. *SB* and *L* performed better than *PP* in terms of contaminants removal and improved adhesive-CFRP interaction, which may enable increased surface wetting. However, as will be shown later, the mechanical and physical surface modification strategies affected in totally different ways in terms of surface topography and morphology.

3.2. Surface topography and morphology

The profile scans and roughness of the treated surfaces are shown in Fig. 3, where the crack growth is along the *x*-direction. The *PP* profiles demonstrate periodic profile peaks and local high-frequency fluctuations. Because of the adhesive viscosity, microscopic asperities may be difficult to be filled thereby preventing intimate molecular contact at the adhesive/CFRP interface. The *SB* surfaces were comparably rough, but did not display high-frequency features. Sandblasting largely increased surface roughness, compared to the baseline *T* surfaces (given in the caption of Fig. 3). Unlike the standard *PP* and *SB* pretreatments, the laser-treated surfaces displayed much lower roughness along the fiber direction, especially at a higher fluence (*L*2), because the surface epoxy was removed and the carbon fibers were exposed. However, the profile scans can be distorted by the finite size of the scanning stylus tip (5 μm). The nominal radius of carbon fibers was 7 μm, and the gaps between the fully exposed fibers were even smaller.

High-resolution observations under SEM were performed to have qualitative assessment of induced morphological modifications, which are shown in Fig. 4. The removal of the peel-ply from the CFRP surface should have exposed fresh epoxy that would enable enhanced adhesive bonding [15]. However, the SEM analyses indicated that the epoxy fracture was limited to the boundary of the imprinted peel-ply patches. The characteristics of the surface created by the peel-ply removal strongly depended on the interaction between the laminate surface matrix and the dry peel-ply fabric during curing. The XPS scan results indicated that, although the texture induced by the peel-ply fabrics increased the surface roughness, the final CFRP featured residual silicon and the limited concentration of functional groups. Therefore, the epoxy fracture was limited and the surface displayed poor adhesion as shown later in mechanical results, which is consistent with the previous work [15]. The *SB* pretreatments resulted in rough surfaces, but several locations also featured damaged carbon fibers. Additional SEM images demonstrated a variable surface morphology, which originated from the difficulty in precisely controlling of such manual processes. The *L*1 surfaces demonstrated partially exposed fibers and micro-scale residual particles, which may have represented products from photo-thermal reactions induced by the laser irradiation. The residual particles produced isolated peaks in the surface profiles (the red arrow in the *x*-

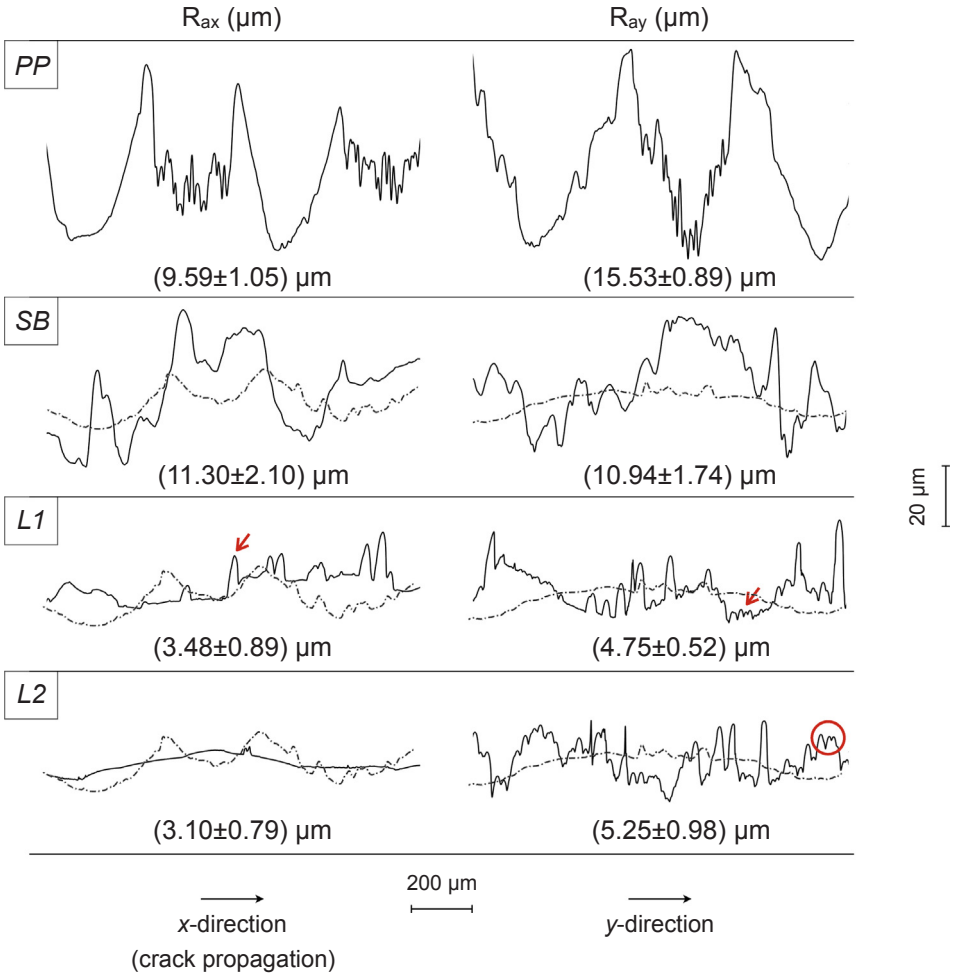

Fig. 3. Typical profile scans and average surface roughness for *PP*, *SB*, *L*1, and *L*2 surfaces. The arrows point to the residual particles (left) and partially exposed fibers (right) on the *L*1 surface. The circle indicates a possible incorrect profile, due to the small gaps between the fibers and the finite size of the scanning probe. The dashed curves show profile scans of the Teflon surfaces: R_{ax} = (3.15 ± 0.74) μm and R_{ay} = (2.97 ± 0.98) μm. (For interpretation of the references to color in this figure legend, the reader is referred to the web version of this article.)

direction profile in Fig. 3), while the partially exposed fibers created high-frequency fluctuations (the red arrow in the *y*-direction profile in Fig. 3). The *L*2 surfaces featured fully exposed carbon fibers as a result of the higher pulse fluence (3.6 J/cm^2), which also led to a drastic reduction in R_{ax}, whereas R_{ay} was very similar to that obtained on the *L*1 surfaces. The *L*2 surface featured loose fibers that could be easily detached.

3.3. Fracture toughness

Typical global responses recorded in DCB tests, which are reported in Fig. 5, consisted of an initial linear elastic region, corresponding to the bending of the beam with the initial crack length a_0, followed by a crack propagation region, which displayed a softening response. The resulting propagation fracture toughness, G_{Ic}, is given as a function of the crack length in Fig. 5 inserts. The overall set of mechanical tests provide values of G_{Ic} in the range of (0.2–1.4) kJ/m^2, which is consistent with previous works on adhesively bonded CFRP laminates [31–33]. Calculation of G_{Ic} was not possible for the baseline *T* surfaces because brittle failure (unstable stick-slip with substantial load jumps) occurred in all tests. Thus, the flat *T* interface led to weak bonding and, for this reason, no results are shown for the *T* surfaces in Fig. 5. It can be concluded that the standard *PP* and *SB* pretreatments defined the lower and upper bounds, respectively, of the mode I fracture toughness. For given applied opening displacement, the *SB* specimens featured a limited crack propagation compared to *PP*, thus indicating a stronger bonding and higher energy dissipation. The results obtained following the *L*1 and *L*2 pretreatments performed better than *PP*, but worse than *SB*. Moreover, increased scattering was also recorded because isolated sudden load drops occurred in the post-peak region, especially at the *L*2 interfaces due to fully exposed carbon fibers.

3.4. Analysis of failure mechanisms

3.4.1. Optical microscopy

Optical microscopy was performed on the fracture surfaces to shed light on the results of mechanical tests, and the observations are reported in Fig. 6, along with a summary plot of the fracture toughness against the atomic concentration of Si. The observed interfacial failure of the *PP* and *T* specimens, which featured the highest atomic concentration of Si and the smallest concentration of polar groups, was caused by the weak adhesive-substrate interactions. Moreover, the *T* surface had very low roughness and was less amenable to mechanical interlocking, which explained the immediate failure and low resistance to crack growth that were observed. The *PP* surfaces were much rougher and resisted debonding well, leading to an enhanced toughness, G_{Ic}^{PP} = 0.17 ± 0.02 kJ/m^2. Yet, the *PP* surfaces were the least tough of all the probed surface conditions. The low fracture toughness probably originated from the chemistry of the *PP* surfaces, which could have been affected by the peel-ply material and the release agent used to

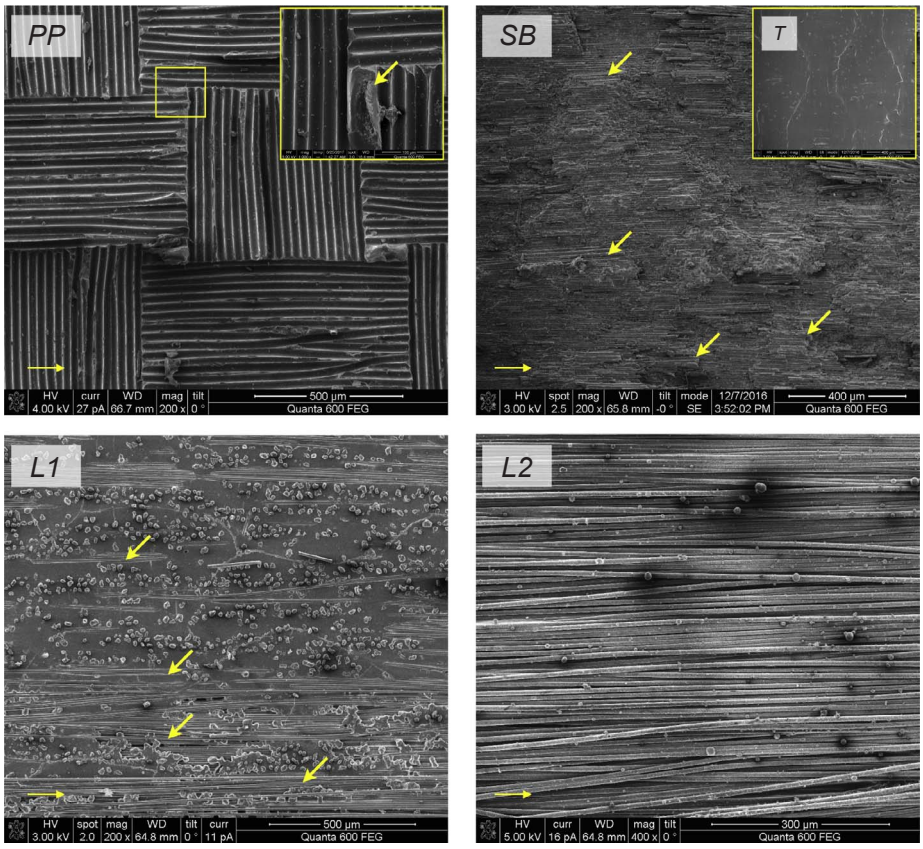

Fig. 4. Morphology of uniform treatments under SEM secondary electron imaging for *PP*, *SB*, *L*1, and *L*2 surfaces. The insert in *PP* indicates a location where peel-ply removal led to the exposure of fresh epoxy, while the insert in *SB* shows the original featureless Teflon interface. (For interpretation of the references to color in this figure legend, the reader is referred to the web version of this article.)

facilitate its removal after curing. Because the manufacturer was reluctant to disclose detailed information about the fabric composition, it was not possible to investigate this point. The *SB* surfaces displayed the highest fracture toughness, *i. e.*, $G_{Ic}^{SB} = 1.13 \pm 0.06$ kJ/m^2. More energy was absorbed with respect to the previous case, *PP* and *T*, as verified by the observed stress "withening", which corresponded to a large adhesive deformation.

The laser-treated surfaces, *L*1 and *L*2, provided distinct mechanical responses. A similar mechanism as the *SB* surfaces was observed in the *L*1 specimens, which also demonstrated the high fracture toughness, *i. e.*, $G_{Ic}^{L1} = 0.75 \pm 0.10$ kJ/m^2. On the other hand, *L*2 featured a relative low fracture toughness, *i. e.*, $G_{Ic}^{L2} = 0.33 \pm 0.17$ kJ/m^2. Optical observations of the *L*2 fracture surfaces also indicated the occurrence of failure at the adhesive/fiber interface. Moreover, areas of imperfect wetting and adhesive penetration were observed, which are indicated by arrows in Fig. 6. For the *T*, *L*1, and *SB* surfaces, the fracture toughness scaled with the atomic concentration of Si. These surfaces can be compared because they involve the presence of an epoxy or a mixture of epoxy and exposed fibers, while *L*2 has a different morphology, as noted previously in Section 3.2.

3.4.2. SEM imaging

Secondary electron imaging was carried out using SEM to resolve the details of the failure process and the results are reported in Fig. 7. Consistent with the optical observations, the *PP* surfaces experienced interfacial failure, with limited cohesive failure occurring, mainly at the boundary of the imprinted peel-ply patches, indicating a detrimental effect of the peel-ply on the surface to be bonded. An analysis of the baseline *T* and *PP* fracture surfaces confirmed that there was poor adhesion between the resin material and the peel-ply fabric. As a result, the functional groups of the uncured pre-preg made contact with the low-energy surface of the peel-ply fabric and, consequently, a similar

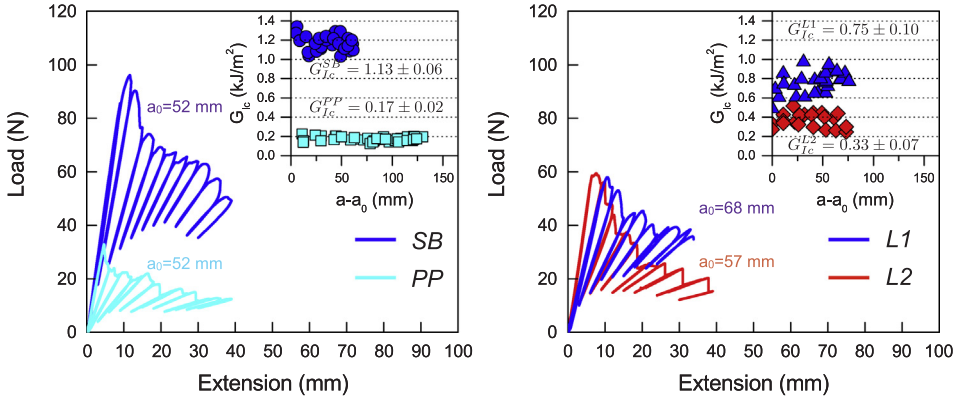

Fig. 5. Typical global responses recorded during the DCB tests. The inserts show the propagation fracture toughness as determined by using the compliance calibration method. (For interpretation of the references to color in this figure legend, the reader is referred to the web version of this article.)

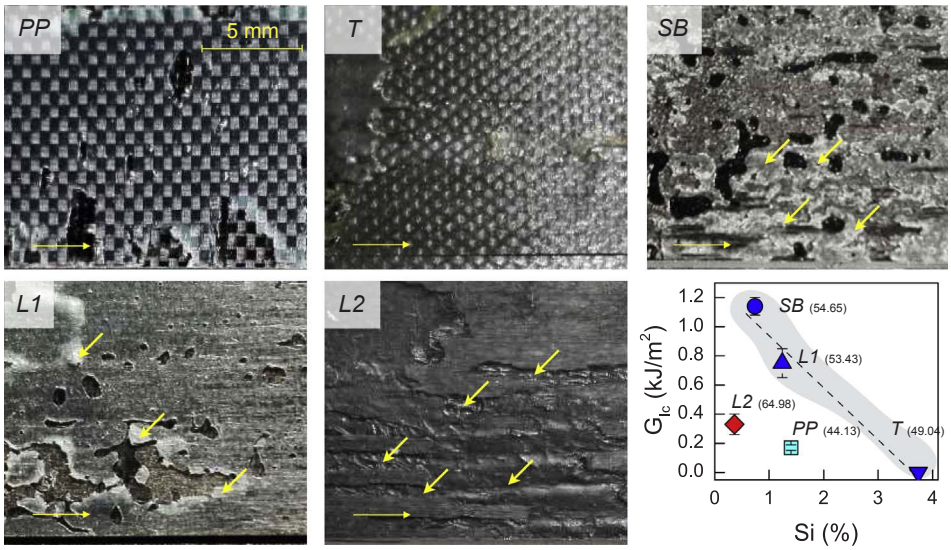

Fig. 6. Optical observations of fracture surfaces and experimental fracture toughness determined from the DCB tests as a function of the atomic concentration of Si. Concentration of total polar functional groups (C−O, C═O, and O−C═O) are shown in the brackets. Crack propagation is from left to right. (For interpretation of the references to color in this figure legend, the reader is referred to the web version of this article.)

peel-ply texture with low surface energy was also generated on the resin side (*i. e.*, bonding surface). The *SB* fracture surfaces revealed the occurrence of cohesive failure, and surface damage in the form of broken carbon fibers from the sandblasting process. Some adhesive porosity, probably originating from the high roughness of the substrate and the resulting entrapped air, was also observed.

Laser irradiation with a low fluence (*L1*) led to improved adhesion at the adhesive/CFRP interface and some degree of cohesive failure, as indicated by the arrows in Fig. 7. There were a few broken fibers because the treatment led to only partial fiber exposure. An analysis of the *L2* surfaces indicated that, because the polymer resin was removed, the surface fibers were isolated from the bulk material. Thus, the crack path was diverted to the adhesive/fiber interface. The weak response is believed to be the result of the poor penetration of the liquid adhesive within fibers and the relative ease with which the loose surface fibers could be detached from the substrate. Similar conclusions were drawn elsewhere [12], where the full removal of the surface matrix led to the formation of a weak boundary layer at the adhesive/exposed-fiber interface, which lowered the shear strength of the joints compared to laser cleaning. In order to enhance adhesive penetration, an additional batch of specimens was fabricated, where the applied pressure during curing was increased from 0.075 bar to 1 bar using the hydraulic hot

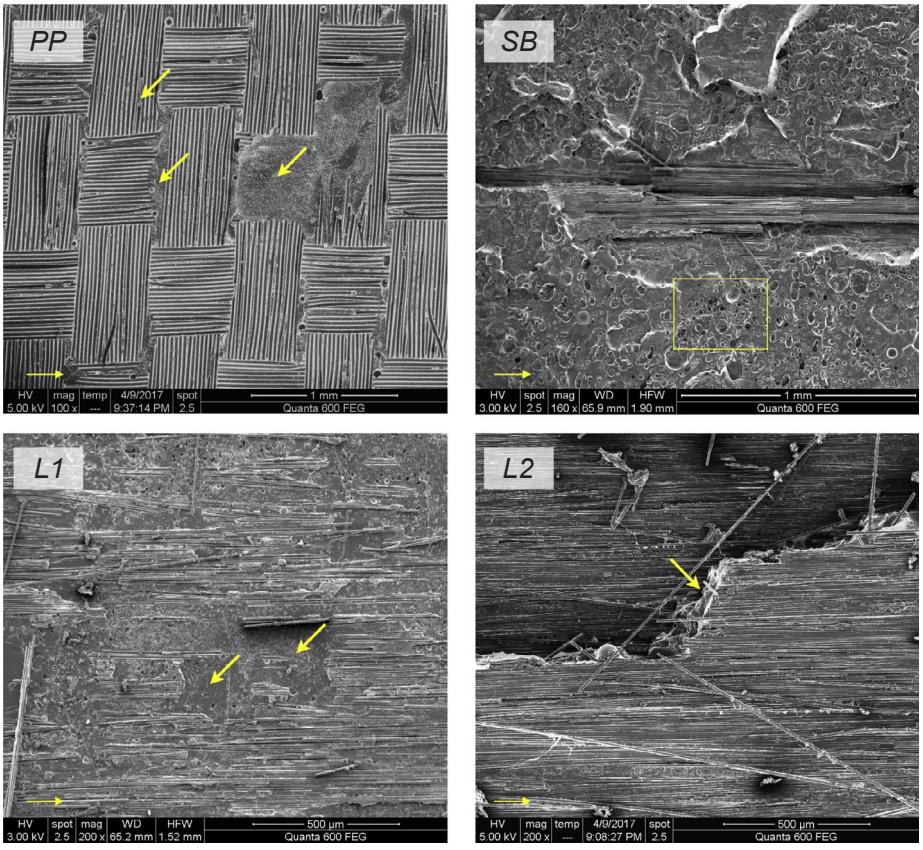

Fig. 7. SEM images of the fracture surfaces on *PP*, *SB*, *L1*, and *L2*. Crack propagation is from left to right. (For interpretation of the references to color in this figure legend, the reader is referred to the web version of this article.)

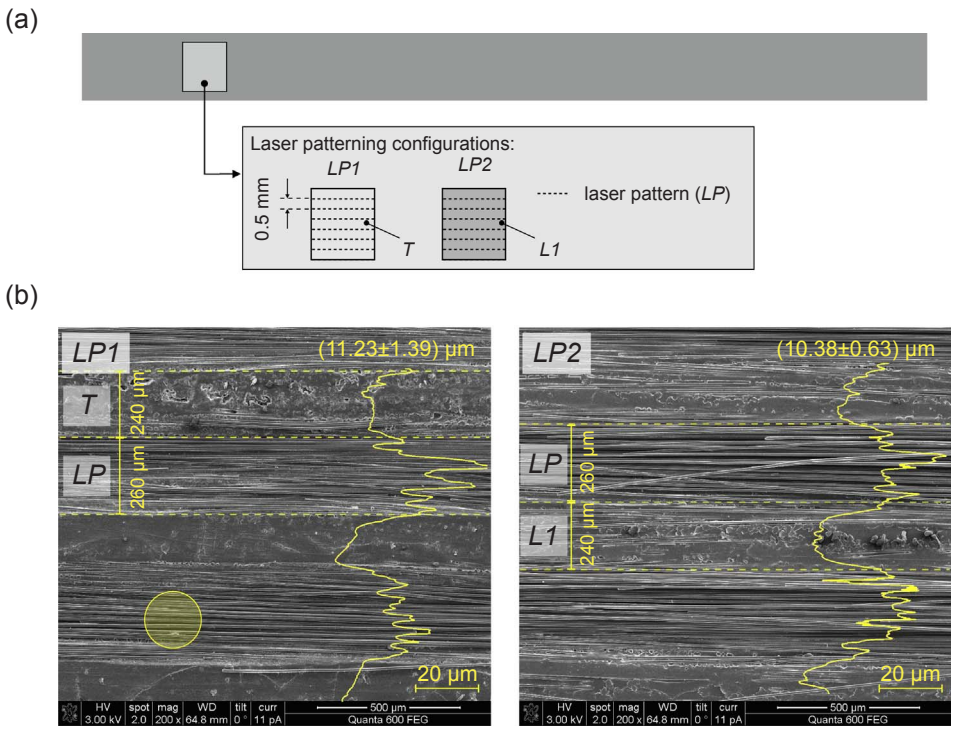

Fig. 8. (a) Schematic of patterned surface pretreatments *LP1* and *LP2*. (b) Morphology of patterned treatments under SEM secondary electron imaging. The images also feature profile scans and corresponding surface roughness perpendicular to the fiber direction. (For interpretation of the references to color in this figure legend, the reader is referred to the web version of this article.)

press machine at the room temperature. However, the results did not display a significant improvement in the fracture toughness, since the differences with respect to the previous batch were within the range of experimental uncertainty. Therefore, the poor wetting of the specific liquid adhesive on the carbon fibers can be hardly improved by the fabrication revisions.

3.5. Effects of laser-based surface patterning

Two laser-based patterning strategies were developed, in order to roughen the adhesive/CFRP interface, increase the contact area, and promote mechanical interlocking. The treatments feature the same pulse fluence, $F_p = 9.1$ J/cm^2, to create surface trenches parallel to the fiber orientation (*x*-direction). A schematic is provided in Fig. 8(a). In one case, *LP*1, the patterns are made on the baseline *T* surface; in the second case, *LP*2, they are made on the *L*1 surface, which provided a better mechanical response in terms of the fracture toughness. The centerline-to-centerline spacing between the trenches was constant at 500 µm. SEM observations of the surface morphology are reported in Fig. 8(b). The profile scans along the *y*-direction were overlapped with the corresponding SEM images to resolve the surface topography in the direction perpendicular to the crack propagation. This combined analysis demonstrated that, due to the thermal interaction between the pulsed laser irradiation and the epoxy resin, the actual trench width was 260 µm, slightly larger than the spot size, and the depth was bell-shaped. Surface conditions within the trench were similar to those of the *L*2 surfaces, but the higher pulse fluence allowed deeper trenches to be obtained in a single pass with limited fiber damage. Fully exposed fibers in the trenches may have provided additional toughening in the form of fiber bridging, as also reported in [22], but this point needs to be assessed after mechanical tests.

Before further mechanical investigation of these laser-based surface patterning, three-point bending tests were performed to evaluate the effects of the surface material removal on the composite stiffness and mechanical strength. A unidirectional CFRP plate was cut into 40 × 6 × 2 mm^3 slices, as shown in Fig. 9. Five original *T* specimens and five *LP*1 specimens were tested under displacement control using the three-point bending fixture on a tensile stage (5 kN Tensile/

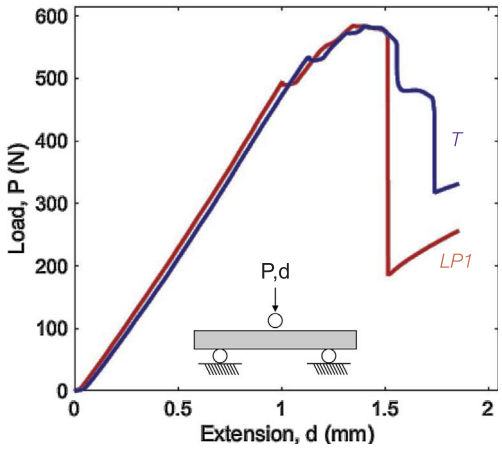

Fig. 9. Typical global responses of *T* and *LP*1, and the schematic of three-point bending tests are shown in the insert. (For interpretation of the references to color in this figure legend, the reader is referred to the web version of this article.)

Compression Module, Kammrath & Weiss, Dortmund, Germany). The support span of the bending fixture was 30 mm, and the displacement loading rate was 0.5 µm/s. Typical global responses obtained in mechanical tests are reported in Fig. 9. Results showed that *T* surfaces had a flexural modulus of 71.35 ± 4.46 GPa, and a flexural strength ([34]) of 1.08 ± 0.06 GPa. While *LP*1 surfaces had a flexural modulus of 67.61 ± 3.31 GPa, and a flexural strength of 1.02 ± 0.05 GPa. The results of mechanical tests before and after the laser pretreatment are very close. Therefore, the material removal associated to laser surface irradiation did not induce significant variations in the strength and bending behavior of unidirectional laminates.

The global responses recorded during the DCB tests and the resulting propagation fracture toughness are reported in Fig. 10. Laser patterning improved the fracture toughness, which reached almost the same level as the *SB* surfaces ($G_{Ic}^{SB} = 1.13 \pm 0.06$ kJ/m^2). The improvement may be associated with the mechanisms of crack growth and failure across the patterned interfaces. *In situ* optical observations of the crack propagation were carried out using a high-resolution camera and

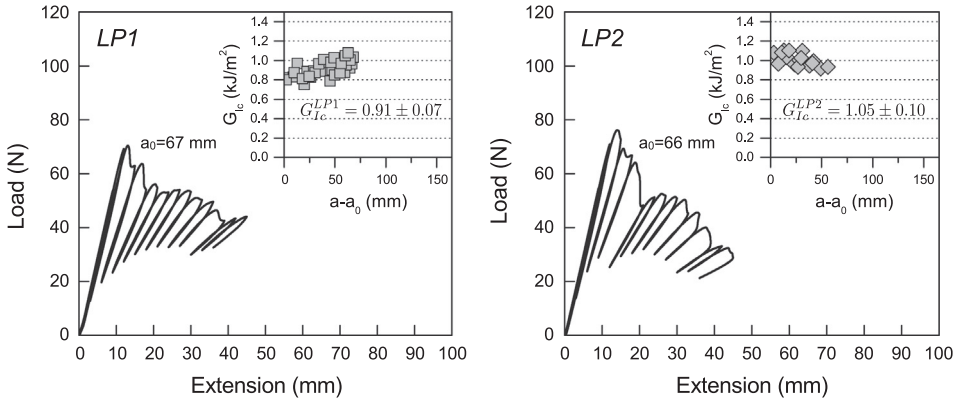

Fig. 10. Typical global responses recorded during the DCB tests and the corresponding fracture toughness of patterned treatments *LP*1 and *LP*2.

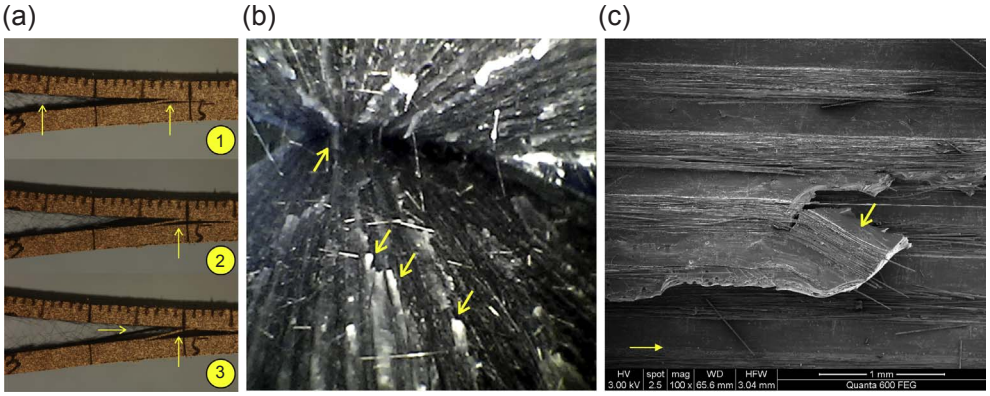

Fig. 11. (a) Optical microscopy images of the crack propagation on one *LP*1 surface recorded during the DCB tests, which show fiber bridging and both the formation and the subsequent failure of adhesive ligaments; (b) *in situ* image of the fracture surface in the crack wake, which shows broken (downward arrows) and unbroken (upward arrow) ligaments; (c) SEM image of a broken adhesive ligament. (For interpretation of the references to color in this figure legend, the reader is referred to the web version of this article.)

an industrial endoscope (CMOS Omnivision OV6946, Precision Optics Corporation Inc., MA, USA) with 400 × 400 pixels resolution. Post-failure SEM imaging of fractured surfaces was also performed. These observations are all provided in Fig. 11. Fig. 11(a) shows the various stages of crack propagation in one *LP*1 specimen. At stage ①, bridging fibers are visible in the wake of the crack, as well as an adhesive ligament developed following the adhesive debonding. At stage ②, some broken fibers are observed, while the size of the adhesive ligament is further increased. As the debonding progresses to stage ③, more fibers are seen and new adhesive ligaments are formed as others are broken. Images of the crack wake, captured through the endoscope, confirm these observations and show multiple instances of broken (downward arrows) and unbroken (upward arrow) adhesive ligaments. The stress "whitening" due to the severe deformation of the epoxy and isolated bridging fibers are also shown. Overall, the fracture surfaces are quite rough and feature several broken ligaments, which appear to have some orientation toward the direction of crack propagation. The SEM image of a broken ligament is presented in Fig. 11(c). The failure process may have contributed to the enhanced fracture toughness. The *LP2* surfaces (not shown) exhibited a similar failure behavior to *LP*1 but more broken fibers were exposed due to the higher toughness of the *L1* pretreatment prior to the patterning.

The experimental mode I fracture toughness reported earlier for the uniform surface pretreatments was used in conjunction with the area fraction of the treated materials to correlate the toughness of the patterned interfaces using the basic rule of mixture:

$$G_{Ic}^{m} = G_{Ic}^{1} \cdot \varphi_1 + G_{Ic}^{2} \cdot \varphi_2, \tag{4}$$

where G_{Ic}^{1} and G_{Ic}^{2} are the fracture toughnesses of surfaces 1 and 2, respectively, and φ_1 and φ_2 are the corresponding area fractions. A representative area was extracted from the treated surfaces, as shown in the highlighted region of Fig. 12(a). Since trenches developed along the *x*-direction, the length ratio of the different regions (shown in the cross-view schematic) gave the area fraction. Based on the surface profile, the depth of the trench (d) was 50 μm and the width (l_{trench}) was 260 μm. Therefore, assuming an arc shape, the corresponding length (l_{arc}) was estimated to be 285 μm. Combined with the width of the "flat" region, l_{flat} = 240 μm, the area fraction of the trench was calculated as $\varphi = l_{arc}/(l_{arc} + l_{flat})$ = 54.3%. It is reasonable to assume that the fracture toughness of the trench region was the same as that of *L2*. Therefore, the rule of mixture for the *LP*1 surfaces was calculated by $G_{Ic}^{1} = G_{Ic}^{L2}$, φ_1 = 54.3%, $G_{Ic}^{2} = G_{Ic}^{T}$, φ_2 = 45.7%, and the rule-of-mixture fracture toughness for *LP*2 was calculated as $G_{Ic}^{1} = G_{Ic}^{L2}$, φ_1 = 54.3%, $G_{Ic}^{2} = G_{Ic}^{L1}$, φ_2 = 45.7%. As shown in Fig. 12(b), *L*2, *L*1 and *SB* are located on the dashed line because they were uniform pretreatments. On the other hand, the patterned interfaces, *LP*1 and *LP*2, deviate from the rule-of-mixture prediction, achieving higher toughness than this linear combination and the same performance as sandblasting (*SB*). The significant enhancement of the experimental fracture toughness compared to the rule-of-mixture prediction may be attributed to several factors. First, a very rough R_{ay} is conducive to mechanical interlocking across the crack propagation direction. Second, the detachment of the adhesive layers within the trench-shape region enhanced energy dissipation through friction. Finally, loose fibers weakened the interface, but also promoted fiber bridging and the formation of adhesive ligaments. However, the improvement of the fracture toughness from *LP*1 to *LP*2 was not significant, although G_{Ic}^{T} was much lower than G_{Ic}^{L1}. Considering the similar failure behavior involving bridging fibers and adhesive ligaments, it is reasonable to conclude that patterning has played a much more important role in interfacial toughening, which requires further investigations in the following work.

4. Conclusions and closing remarks

In this study, the effects of surface pretreatments using pulsed CO_2

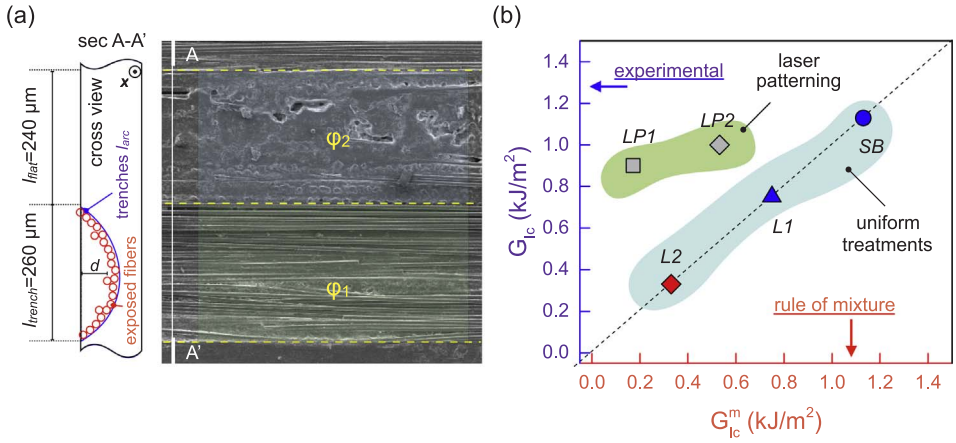

Fig. 12. (a) Schematic of the procedure employed to calculate area fraction; (b) comparison between the experimental values of fracture toughness (*y*-direction) and the corresponding predictions obtained using the rule of mixture (*x*-direction). (For interpretation of the references to color in this figure legend, the reader is referred to the web version of this article.)

laser irradiation on mode I fracture toughness of adhesively bonded composite joints were evaluated. The mechanical behavior was assessed through double cantilever beam (DCB) tests. The confluence of damage mechanisms in the laser-patterned surfaces, not normally observed in uniformly treated interfaces, allowed the fracture toughness to exceed the predictions based on a simple rule of mixture. The large interfacial area associated with the trench-shaped patterns effectively deflected the cracks and generated extrinsic mechanisms of energy dissipation, such as toughening by unbroken fibers and uncracked adhesive ligaments. Fiber bridging and ligaments provided nonlinear deformation mechanisms allowed the inherently brittle interface to deform inelastically, redistribute the stresses around defects, and dissipate energy. The proposed strategy can be customized for different composites applied to the aerospace industry due to the high precision, reproducibility, and potential automation of the pulsed laser irradiation system.

Acknowledgement

The research reported in this publication was supported by funding from King Abdullah University of Science and Technology (KAUST).

References

[1] Schmid Fuertes T, Kruse T, Körwien T, Geistbeck M. Bonding of CFRP primary aerospace structures, a discussion of the certification boundary conditions and related technology fields addressing the needs for development. Compos Interf 2015;22(8):795–808. http://dx.doi.org/10.1080/09276440.2015.1077048.

[2] Russell J. Composites affordability initiative: transitioning advanced aerospace technologies through cost and risk reduction. AMMTIAC Quart 2006;1(3):3–6.

[3] Katnam K, Da Silva L, Young T. Bonded repair of composite aircraft structures: a review of scientific challenges and opportunities. Prog Aerospace Sci 2013;61:26–42. http://dx.doi.org/10.1016/j.paerosci.2013.03.003.

[4] Lu J-H, Youngblood J. Adhesive bonding of carbon fiber reinforced composite using uv-curing epoxy resin. Compos Part B: Eng 2015;82:221–5.

[5] Heshmati M, Haghani R, Al-Emrani M. Environmental durability of adhesively bonded FRP/steel joints in civil engineering applications: state of the art. Compos Part B: Eng 2015;81:259–75.

[6] Korta J, Mlyniec A, Uhl T. Experimental and numerical study on the effect of humidity-temperature cycling on structural multi-material adhesive joints. Compos Part B: Eng 2015;79:621–30.

[7] Korayem A, Li C, Zhang Q, Zhao X, Duan W. Effect of carbon nanotube modified epoxy adhesive on CFRP-to-steel interface. Compos Part B: Eng 2015;79:95–104<https://www.scopus.com/inward/record.uri?eid=2-s2.0-84928905621&doi=10.1016%2fj.compositesb.2015.03.063&partnerID=40&md5=cce22272cd5512fa178ab88959356646>.

[8] Galvez P, Quesada A, Martinez M, Abenojar J, Boada M, Diaz V. Study of the behaviour of adhesive joints of steel with CFRP for its application in bus structures. Compos Part B: Eng 2017;129:41–6<https://www.scopus.com/inward/record.uri?eid=2-s2.0-85026435166&doi=10.1016>.

[9] Fischer F, Kreling S, Dilger K. Laser surface pre-treatment of carbon fiber-reinforced plastics (CFRPs) for adhesive bonding. In: Laser surface modification and adhesion; 2014. p. 103–38 [chapter 3]. doi:http://dx.doi.org/10.1002/9781118831670.ch3.

[10] Hartwig A, Vit G, Dieckhoff S, Hennemann O. Surface treatment of an epoxy resin by CO_2 laser irradiation. Die Angew Makromol Chem 1996;238:177–89.

[11] Bénard Q, Fois M, Grisel M. Peel ply surface treatment for composite assemblies: chemistry and morphology effects. Compos Part A: Appl Sci Manuf 2005;36(11):1562–8. http://dx.doi.org/10.1016/j.compositesa.2005.02.012.

[12] Bénard Q, Fois M, Grisel M, Laurens P. Surface treatment of carbon/epoxy and glass/epoxy composites with an excimer laser beam. Int J Adhes Adhes 2006;26(7):543–9. http://dx.doi.org/10.1016/j.ijadhadh.2005.07.008.

[13] Zaldivar R, Kim HH, Steckel G, Nokes J, Morgan B. Effect of processing parameter changes on the adhesion of plasma-treated carbon fiber reinforced epoxy composites. J Compos Mater 2010;44(12):1435–53. http://dx.doi.org/10.1177/0021998309355846.

[14] Balart J, Fombuena V, España J, Sánchez-Nácher L, Balart R. Improvement of adhesion properties of polypropylene substrates by methyl methacrylate uv photografting surface treatment. Mater Des 2012;33:1–10.

[15] Holtmannspötter J, Czarnecki JV, Wetzel M, Dolderer D, Eisenschink C. The use of peel ply as a method to create reproduceable but contaminated surfaces for structural adhesive bonding of carbon fiber reinforced plastics. J Adhes 2013;89(2):96–110. http://dx.doi.org/10.1080/00218464.2012.731828.

[16] Palmieri F, Hopkins J, Wohl C, Lin Y, Connell J, Belcher M, et al. Laser surface preparation of epoxy composites for secondary bonding: optimization of ablation depth.

[17] Jölly I, Schlögl S, Wolfahrt M, Pinter G, Fleischmann M, Kern W. Chemical functionalization of composite surfaces for improved structural bonded repairs. Compos Part B: Eng 2015;69:296–303. http://dx.doi.org/10.1016/j.compositesb.2014.10.020.

[18] Palmieri F, Belcher M, Wohl C, Blohowiak K, Connell J. Laser ablation surface preparation for adhesive bonding of carbon fiber reinforced epoxy composites. Int J Adhes Adhes 2016;68:95–101.

[19] Zaldivar R, Kim H, Steckel G, Patel D, Morgan B, Nokes J. Surface preparation for adhesive bonding of polycyanurate based fiber reinforced composites using atmospheric plasma treatment. J Appl Polym Sci 2011;120(2). http://dx.doi.org/10.1002/app Available from: arXiv: 1206.452.

[20] Serrano J, Urena A, Lazcano Urena S, Blanco Verala T. New approach to surface preparation for adhesive bonding of aeronautical composites: atmospheric pressure plasma. Studies on the pretreatment lifetime and durability of the bondline. Compos Interf 2015;6440(July):22–6. http://dx.doi.org/10.1080/09276440.2015.1056671.

[21] Kreling S, Fischer F, Delmdahl R, Gäbler F, Dilger K. Analytical characterization of CFRP laser treated by excimer laser radiation. Phys Proc 2013;41:282–90.

[22] Kruse T, Koerwin T, Heckner S, Geistbeck M. Bonding of CFRP primary aerospace structures - crackstoppings in composite bonded joints under fatigue. In: ICCM 20 20th international conference on composite materials (July); 2015. p. 19–24.

[23] Yokozeki T, Ishibashi M, Kobayashi Y, Shamoto H, Iwahori Y. Evaluation of adhesively bonded joint strength of CFRP with laser treatment. Adv Compos Mater 2016;25(4):317–27.

[24] Almuhammadi K, Selvakumaran L, Alfano M, Yang Y, Bera T, Lubineau G. Laser-based surface preparation of composite laminates leads to improved electrodes for electrical measurements. Appl Surface Sci 2015;359:388–97.

[25] Reitz V, Meinhard D, Ruck S, Riegel H, Knoblauch V. A comparison of ir- and uv-laser pretreatment to increase the bonding strength of adhesively joined aluminum/CFRP components. Compos Part A: Appl Sci Manuf 2017;96:18–27.

[26] Hernandez E, Alfano M, Lubineau G, Buttner U. Improving adhesion of copper/epoxy joints by pulsed laser ablation. Int J Adhes Adhes 2016;64:23–32. http://dx.doi.org/10.1016/j.ijadhadh.2015.10.003.

[27] Standard test method for mode I interlaminar fracture toughness of unidirectional fiber-reinforced polymer matrix composites. ASTM Internat.

[28] Qian Y, Wei P, Jiang P, Hao J, Du J. Preparation of hybrid phosphamide containing polysilsesquioxane and its effect on flame retardancy and mechanical properties of polypropylene composites. Compos Part B: Eng 2013;45(1):1541–7. http://dx.doi.org/10.1016/j.compositesb.2012.09.064.

[29] Markatos D, Tserpes K, Rau E, Markus S, Ehrhart B, Pantelakis S. The effects of manufacturing-induced and in-service related bonding quality reduction on the

mode-i fracture toughness of composite bonded joints for aeronautical use. Compos Part B: Eng 2013;45(1):556–64.
[30] Markatos D, Tserpes K, Rau E, Brune K, Pantelakis S. Degradation of mode-I fracture toughness of CFRP bonded joints due to release agent and moisture pre-bond contamination. J Adhes 2014;90(2):156–73. http://dx.doi.org/10.1080/00218464.2013.770720.
[31] Fernandes R, de Moura M, Moreira R. Effect of moisture on pure mode i and ii fracture behaviour of composite bonded joints. Int J Adhes Adhes 2016;68:30–8.
[32] Yavas D, Shang X, Hong W, Bastawros A. Utilization of nanoindentation to examine bond line integrity in adhesively bonded composite structures. Int J Fract 2016:1–12.
[33] Stefanov T, Ryan B, Ivanković A, Murphy N. Mechanical bulk properties and fracture toughness of composite-to-composite joints of an elastomer-toughened ethyl cyanoacrylate adhesive. Int J Adhes Adhes 2016;68:142–55.
[34] Standard test methods for flexural properties of unreinforced and reinforced plastics and electrical insulating materials. ASTM Internat. doi:http://dx.doi.org/10.1520/D0790-17.